Review

Not peer-reviewed version

Atmospheric Icing Mitigation on Unmanned Aerial Vehicles: Electrothermal Strategies and Functional Materials for Operational Safety Under Known Icing Conditions

Paula Natalia Lopez , Camila Andrea Gonzalez , Richard Giovanni Avella *

Posted Date: 13 May 2026

doi: 10.20944/preprints202605.0798.v1

Keywords: atmospheric icing; UAV; propellers; electrothermal modelling, superhydrophobic coatings; functional composites; anti-icing; de-icing, supercooled water; low Reynolds number

 doi:10.20944/preprints202605.0798.v1

Review

Atmospheric Icing Mitigation on Unmanned Aerial Vehicles: Electrothermal Strategies and Functional Materials for Operational Safety Under Known Icing Conditions

Paula Natalia Lopez, Camila Andrea Gonzalez and Richard Giovanni Avella *

Fundación Universitaria Los Libertadores, Faculty of Engineering and Basic Sciences, Bogotá, Colombia
* Correspondence: rgavellas@unal.edu.co

Abstract

Atmospheric icing is one of the most critical meteorological hazards for unmanned aerial vehicles (UAV), whose operation under adverse conditions—high latitudes, elevated altitudes, long-endurance missions without pilot intervention—particularly exposes them to ice accumulation on aerodynamic surfaces and propellers. Unlike manned aviation, where this phenomenon has been extensively studied and regulated, a significant knowledge gap exists in the UAV domain that limits the development of effective protection systems adapted to energy constraints. This article provides an integrated review of atmospheric ice formation mechanisms, their specific effects on UAV propellers, and the two most promising mitigation approaches: electrothermal modelling for the optimisation of electric heating systems, and the development of functional surface materials, including superhydrophobic coatings (SHC), composites with conductive nanofillers (graphene, carbon nanotubes), and piezoelectric actuators. The analysis demonstrates that hybrid systems combining passive and active strategies managed by intelligent control represent the most viable solution for extending UAV operational envelopes under known icing conditions, with a potential reduction in anti-icing energy consumption exceeding 40 % compared to conventional continuous heating. Key research gaps are identified, and a prioritised future research agenda is proposed to support the development of certifiable anti-icing systems for rotary-wing UAV platforms.

Keywords: atmospheric icing; UAV; propellers; electrothermal modelling, superhydrophobic coatings; functional composites; anti-icing; de-icing, supercooled water; low Reynolds number

1. Introduction

Airframe icing constitutes one of the most severe meteorological hazards in aviation, encompassing a complex coupling between atmospheric microphysics, surface thermodynamics, and aerodynamic performance degradation. When an aircraft traverses a cloud containing supercooled large droplets (SLD) or encounters freezing precipitation, impinging water droplets freeze upon contact with exposed surfaces, forming accretion structures whose geometry—rime, glaze, or mixed ice—depends critically on the liquid water content (LWC), median volumetric diameter (MVD), freestream temperature (T_∞), and collection efficiency of the surface [1,2]. The thermodynamic foundation of this process was formalised by Messinger [1], whose steady-state energy balance at the impingement surface remains the canonical framework for icing accretion modelling. Subsequent refinements by Ruff and Berkowitz [3] and the LEWICE [4] and FENSAP-ICE [5] computational codes have extended this formulation to three-dimensional unsteady multi-step accretion scenarios.

The aerodynamic consequences of ice accretion are well documented for transport-category aircraft. Progressive accumulation on lifting surfaces disrupts the pressure distribution over the airfoil, induces early boundary-layer separation, and degrades both maximum lift coefficient ($C_{L,\max}$) and

 doi:10.20944/preprints202605.0798.v1

stall margin. The Federal Aviation Administration (FAA) Advisory Circular AC 91-74B establishes that intercycle and residual ice formations can reduce $C_{L,\max}$ by up to 30 % and increase profile drag by more than 40 %, depending on ice shape, surface roughness, and chord Reynolds number [6]. Lynch and Khodadoust [7] conducted an exhaustive meta-analysis of icing wind-tunnel experiments and confirmed reductions of up to 50 % in $C_{L,\max}$ and drag increments of 100–200 % for glaze-ice horn geometries on NACA 0012 and 23012 sections, effects directly attributable to the formation of large separation bubbles downstream of the ice horn. The severity of performance penalties is further modulated by ice surface roughness: Bragg et al. [8] demonstrated that even sub-millimetre roughness elements on the leading edge produce a disproportionate loss of lift-curve slope through premature transition and thickening of the turbulent boundary layer, an effect particularly acute at chord Reynolds numbers below 5×10^5.

In the context of unmanned aerial vehicles (UAVs), the icing threat acquires a distinctly critical operational dimension. UAV platforms are expressly designed to operate under conditions that civil aviation systematically avoids: extended-endurance missions over mountainous terrain at night, sustained operations in arctic and sub-arctic theatres, loitering at altitudes presenting elevated concentrations of supercooled water (LWC $> 0.5\,\mathrm{g\,m^{-3}}$), and tactical scenarios where mission abort is operationally impermissible [9,10]. Unlike crewed aircraft, UAVs are equipped with no on-board pilot capable of perceiving anomalous vibration signatures, changes in control response, or progressive increases in power demand; ice-induced degradation therefore has the potential to proceed to structural failure or loss of control without any corrective intervention [9]. The accident record compiled by Hann et al. [11] for small and medium UAVs operating in Scandinavian conditions confirms that icing events are systematically underreported and that available meteorological forecasting tools—designed for transport aircraft with substantially different collection efficiencies—underestimate the icing exposure of small platforms by a significant margin.

The problem is compounded by aerodynamic and structural characteristics intrinsic to small and medium-class UAVs. Their propulsion systems operate at chord Reynolds numbers in the range $Re = 10^4$–10^5, a regime in which laminar separation bubbles are inherently present on uncontaminated surfaces and in which the boundary layer is highly susceptible to the additional disturbances introduced by even sub-millimetre ice roughness [8,12]. Thin aerofoil sections with leading-edge radii of the order of 0.5–2 mm present geometric collection efficiencies substantially higher than those of large-chord surfaces, accelerating accretion rates per unit of atmospheric exposure [13]. An ice layer of only 0.5–1 mm on the leading edge of a propeller blade can reduce the local lift coefficient by 30–40 % and simultaneously increase rotational drag torque, degrading thrust output and propulsive efficiency in a manner entirely disproportionate to that observed on transport-aircraft wings under equivalent atmospheric conditions [8,14]. For multi-rotor platforms, this efficiency loss translates directly into reduced hover endurance and, at critical accumulation levels, into rotor asymmetry that exceeds the authority of the flight-control system [15,16].

Recent experimental and computational investigations have substantially advanced the characterisation of propeller icing on small UAVs. Hann et al. [11] performed systematic icing wind-tunnel tests on a fixed-pitch propeller representative of medium-class UAVs, reporting thrust reductions of up to 35 % and torque increases of 28 % under glaze-ice conditions with $T_\infty = -5\,^\circ\mathrm{C}$ and LWC $= 0.8\,\mathrm{g\,m^{-3}}$. Villeneuve et al. [15] extended these findings to multi-rotor configurations, demonstrating that non-uniform accretion between coaxial rotors induces vibrational imbalances detectable in ESC current signatures, a result with direct implications for sensorless on-board detection. Cao et al. [17] investigated the influence of supercooled large droplets on the aerodynamic performance of UAV aerofoils at low Reynolds numbers, establishing that SLD conditions—defined under FAR Part 25 Appendix O—produce runback ice formations at chord positions beyond 30 % that are not captured by classical Appendix C certification envelopes and that are therefore particularly hazardous for platforms operating in maritime or mountain-wave environments. Computational investigations using FENSAP-ICE [18] and LEWICE [4] have confirmed the qualitative trends observed experimentally

 doi:10.20944/preprints202605.0798.v1

while revealing that numerical predictions diverge appreciably from measurements at the lowest Reynolds numbers ($Re < 5 \times 10^4$), where turbulence model limitations and transitional flow effects introduce non-negligible uncertainty [19].

The development of ice protection systems (IPS) for UAV propellers must reconcile performance requirements with stringent energy constraints, given that propulsion and avionics already consume the largest fraction of onboard battery capacity. Electrothermal systems—the dominant technology in crewed aviation [18]—have been adapted for UAV rotors in pulsed-heating configurations that reduce mean power consumption by 60–75 % relative to continuous heating by exploiting ice-interface temperature transients [15,20]. Passive mitigation through superhydrophobic coatings (SHC) fabricated by nanostructured sol-gel, electrospun polymer, or laser-ablation processes can reduce ice adhesion strength below 25 kPa and shift the dynamic contact angle above 150°, lowering the energy required for ice shedding under centrifugal loading [21]. Piezoelectric actuators—particularly polyvinylidene fluoride (PVDF) films and macro-fibre composites (MFC)—offer a third modality: resonant mechanical excitation of blade structures at frequencies of 100–500 Hz generates shear stresses at the ice interface that exceed adhesion strength with energy expenditures 10–50 times lower than equivalent electrothermal approaches [22,23]. The integration of these three strategies into a hierarchical hybrid architecture, governed by an adaptive controller informed by real-time ice-severity estimates from machine-learning classifiers trained on vibration and thermal signatures, represents the current frontier of the field [24,25].

Despite the operational and scientific relevance of the problem, peer-reviewed literature specifically addressing ice protection for UAV propellers remains sparse relative to the body of knowledge accumulated for fixed-wing transport aircraft and, more recently, wind turbines. The majority of existing studies either extrapolate results from large-chord, high-Reynolds-number configurations whose aerodynamic regimes and thermodynamic boundary conditions differ substantially from those of small-UAV propellers, or focus on detection and characterisation without extending to integrated protection solutions [26]. This knowledge gap, combined with the increasing operational deployment of UAVs in high-latitude and high-altitude theatres where icing encounters are frequent, motivates the present review.

This article examines in an integrated manner: (i) the physical mechanisms governing ice nucleation, droplet impingement, and accretion on UAV propeller blades within low-Reynolds-number aerodynamic regimes; (ii) electrothermal modelling frameworks for the design and energy optimisation of resistive heating elements, including pulsed and zone-controlled architectures; (iii) functional surface materials—superhydrophobic, icephobic, and electro-responsive coatings—as passive and active mitigation strategies; and (iv) the systems-level integration of sensing, actuation, and control layers into hybrid anti-icing architectures compatible with the energy budget of battery-powered UAVs.

The literature search was conducted systematically in Scopus, Web of Science, and Google Scholar using the following Boolean descriptors: *UAV icing*, *drone propeller icing*, *electrothermal anti-icing rotary wing*, *superhydrophobic icephobic coating propeller*, *piezoelectric deicing UAV*, *low Reynolds icing aerodynamics*, *SLD icing small aircraft*, and *UAV ice protection system*. The temporal scope encompassed publications from 1990 to May 2025, with priority assigned to research articles indexed in Q1–Q2 journals in the aerospace engineering and materials science categories (JCR and SJR), as well as technical reports issued by NASA, FAA, EASA, and the Defence Research and Development Canada (DRDC). Grey literature was incorporated exclusively where no peer-reviewed equivalent was available for a specific data point or operational context. After a two-stage relevance and methodological quality screening—applying PRISMA guidelines adapted to engineering review methodology—a corpus of 47 primary sources was retained and constitutes the bibliographic backbone of this work.

The article is structured as follows. Section II presents the systematic literature review and bibliometric characterisation of the field. Section III describes the atmospheric physics of ice formation and the thermodynamic framework governing accretion on rotating surfaces. Section IV analyses

 doi:10.20944/preprints202605.0798.v1

experimentally and computationally validated icing effects on UAV propellers across the relevant Reynolds number range. Section V develops the electrothermal modelling framework, including analytical and finite-element formulations for pulsed heating optimisation. Section VI reviews functional surface material strategies, with emphasis on icephobic coatings and piezoelectric actuation. Section VII presents an integrative discussion of hybrid architectures, control strategies, and open research challenges. Section VIII formulates the principal conclusions and outlines priority directions for future investigation.

2. Literature Review

2.1. Classical Foundations of Aeronautical Icing Research

Systematic research on in-flight icing began in earnest during the 1940s, driven primarily by the NASA Glenn Research Center, which established the Icing Research Tunnel (IRT)—still one of the world's leading experimental facilities—and developed the LEWICE prediction code, a Lagrangian droplet trajectory and ice accretion solver that remains the industry-standard benchmark against which newer computational methods are validated [27]. These foundational works identified the critical combinations of liquid water content (LWC), median volumetric diameter (MVD) and temperature that define the icing envelope subsequently codified in FAR Part 25 Appendix C [28].

Gent et al. [29] provided a seminal multidisciplinary review covering droplet trajectory modelling, thermodynamic phase change at the impingement surface, and ice geometry prediction. Thomas et al. [30] formalised the coupled thermal-aerodynamic energy balance for electrothermal leading-edge heating systems, introducing the concept of the anti-icing heat flux distribution that later works extended to rotary-wing platforms. Bragg et al. [8] conducted an exhaustive survey of iced-aerofoil aerodynamics, quantifying C_L and C_D degradation as a function of accretion geometry across a wide range of Reynolds numbers and demonstrating that even small horn-ice features at the leading edge produce disproportionate penalties at low angles of attack.

2.2. Icing on UAV Platforms: From Early Recognition to Recent Experimental Characterisation

2.2.1. Early and Foundational Work

The operational impact of icing on unmanned platforms was first systematically documented by Siquig [9], who identified thrust loss and propeller imbalance as the primary failure modes and noted the absence of autonomous ice detection as a critical aggravating factor unique to UAV operations. Cao et al. [31] provided an updated review identifying, as a central gap, the inapplicability of high-Reynolds aerodynamic correlations and ice accumulation models—developed for commercial transport aircraft—to UAVs operating at $Re < 10^5$, where laminar separation bubbles and transitional boundary layers fundamentally alter the droplet collection efficiency and heat transfer coefficients.

2.2.2. Low-Reynolds Propeller Icing: Experimental Advances

The past six years have seen a marked acceleration in experimental characterisation of icing on small-scale rotary systems. Hann and Wallisch [11] reviewed more than 100 icing studies and concluded that propeller icing research lags behind fixed-wing UAV icing by approximately a decade, with fewer than 15 experimental datasets available for low-Reynolds propeller ice accretion at the time of publication. Hann et al. [14] further quantified the aerodynamic penalties on multi-rotor platforms, demonstrating C_L losses of 30–40 % consistent with fixed-wing aerofoil data and identifying that asymmetric accretion between blades induces vibration-driven motor failures at timescales shorter than thrust degradation alone.

A milestone experimental campaign was carried out by Müller et al. [32], who designed and tested a full electrothermal Ice Protection System (IPS) for the propeller of a small fixed-wing UAV in an icing wind tunnel, coupling ANSYS FENSAP-ICE conjugate heat transfer (CHT) simulations with experimental validation data. Their results established that existing manned-aviation CHT methods, when applied without modification at low Reynolds numbers, overestimate the convective heat

 doi:10.20944/preprints202605.0798.v1

transfer coefficient at the blade surface, leading to over-conservative IPS designs with unnecessarily high power demands. This finding was subsequently confirmed and extended by Frey et al. [33], who demonstrated through FENSAP-ICE CHT simulations that accounting for laminar-to-turbulent boundary-layer transition reduces predicted anti-icing power requirements by 15–25 % relative to fully turbulent assumptions.

Müller et al. [34] performed a comprehensive experimental characterisation of performance degradation on a 0.53 m diameter propeller under systematic variation of MVD (20, 40 and 60 μm), LWC (0.28–1.12 g/m^3) and temperature (-5, -10, -15 °C) in an icing wind tunnel. Their results revealed that MVD is the dominant parameter: after one minute of icing exposure at MVD = 60 μm, the propeller generated net drag instead of thrust, a result qualitatively consistent with the earlier numerical predictions of Shi et al. [35], who showed using FENSAP-ICE that higher RPM concentrates ice accretion at the blade tip and promotes horn-ice formation characteristic of the glaze regime.

Karpen et al. [24] addressed the integration of airfoil heater elements directly into propeller blades for small multi-rotor drones in an anti-icing configuration, establishing feasibility maps relating required power density (W/cm^2) to LWC and temperature and demonstrating that tip-region heating must deliver at least twice the power density required at mid-span, due to the higher relative velocity and collection efficiency in that region. This result provides the first quantitative design criterion for the non-uniform distribution of resistive elements in UAV propeller blades.

Villeneuve et al. [36] developed and validated an experimental apparatus for icing tests of low-altitude hovering drones and used it to characterise rotor performance degradation under controlled icing conditions, demonstrating that torque increases at a faster rate than thrust decreases, implying that energy-to-thrust efficiency degrades more severely than the thrust coefficient alone would suggest. Harvey et al. [37] extended this investigation to forward-flight configurations in a wind tunnel, establishing that advancing-blade asymmetry generates significantly higher glaze ice accumulation on the leading edge of the advancing blade than on the retreating blade, with consequences for vibration prediction and anti-icing zone prioritisation in UAV systems.

Ercan and Dalkın [38] conducted a full-vehicle experimental investigation of propeller icing on a hovering quadcopter under rime and glaze conditions, confirming at the platform level that larger droplets, lower rotor speeds and lower blade angles of attack lead to faster and more severe thrust losses, and demonstrating that indirect current-monitoring of the ESC (Electronic Speed Controller) provides a viable real-time proxy for ice detection without additional sensing hardware.

Muhammed and Virk [39] provided a systematic literature review focused exclusively on rotary-wing UAVs, covering 87 studies and identifying four major research gaps still unresolved at the time of publication: (i) the absence of standardised low-Reynolds icing envelopes for UAV certification; (ii) the lack of validated numerical methods for rotating aerofoils at $Re < 2 \times 10^4$; (iii) the limited understanding of ice shedding dynamics under centrifugal loading; and (iv) the scarcity of in-flight data from real icing encounters compared to wind-tunnel campaigns.

2.2.3. Thermal Modelling and Electrothermal Optimisation

Liu and Hu [40] provided fundamental experimental data on the unsteady convective heat transfer process over actively icing aerofoil surfaces, establishing that the local Nusselt number can vary by a factor of three along the chord due to laminar separation bubble dynamics, a result of direct relevance to the discretisation strategy of electrothermal models at low Reynolds numbers. Pourbagian and Habashi [18] developed a surrogate-based optimisation framework for electrothermal IPS in transient de-icing mode, demonstrating energy consumption reductions of 40–60 % relative to continuous heating by exploiting the latent heat of fusion at the ice-substrate interface during each heating pulse. Their methodology, originally derived for fixed-wing leading edges at high Reynolds numbers, has been identified as the most complete analytical basis available for adaptation to the UAV propeller context [32].

 doi:10.20944/preprints202605.0798.v1

2.3. Materials and Surfaces for Icing Mitigation

2.3.1. Superhydrophobic and Icephobic Coatings

Mishchenko et al. [41] established the design principles for icephobic nanostructured surfaces based on the Cassie-Baxter wetting state and the repulsion of impacting supercooled droplets. Susoff et al. [42] performed the first systematic screening of icephobic coatings under erosion conditions representative of aviation applications, identifying surface roughness as the dominant parameter governing durability and noting that erosion-induced destruction of the micro-nanostructure responsible for superhydrophobicity can occur within hours of exposure at blade-tip relative velocities exceeding 80 m/s.

This durability limitation has been the central focus of recent research. Nistal et al. [43] reviewed the state of the art in icephobic coating durability, concluding that superhydrophobic surfaces (WCA $>$ 150) consistently fail after repeated icing-deicing cycles under frost formation conditions due to water infiltration into the surface microstructure, restoring the Wenzel wetting state and eliminating icephobicity. Their analysis highlights that the optimal balance between icephobicity and durability is achieved by smooth hydrophobic surfaces ($90° \leq$ WCA $\leq 150°$) rather than superhydrophobic microstructures, a finding that has direct implications for coating selection in UAV propeller applications subject to centrifugal erosion. Complementary work by Wang et al. [44] demonstrated that slippery erosion-resistant polyurethane (SPU) coatings incorporating fluorinated polymer surface-modifying groups achieve ice adhesion strengths below 50 kPa while maintaining structural integrity under simulated leading-edge erosion at 100 m/s, a velocity comparable to UAV blade-tip speeds.

Villeneuve et al. [45] conducted a systematic experimental assessment of icephobic coating effectiveness on a hovering drone rotor, testing three commercial coatings under controlled icing conditions and demonstrating that passive coatings alone reduce ice accretion mass by 20–40 % under rime conditions but are largely ineffective under glaze conditions at LWC $>$ 0.5 g/m^3, underscoring the need for hybrid active-passive architectures. Tu et al. [46] investigated the substrate wettability effects on dynamic ice accretion and shedding over a rotating UAV propeller, showing that hydrophobic surfaces promote earlier ice shedding under centrifugal loading by reducing the critical ice mass threshold for adhesion failure, with implications for the design of passive de-icing strategies.

Han et al. [47] compared superhydrophobic and icephobic hybrid heating strategies on a NACA0012 aerofoil in the Iowa State University Icing Research Tunnel, demonstrating that the superhydrophobic hybrid reduces required heater power by more than 80 % relative to the conventional electrothermal anti-icing strategy alone, principally through droplet bounce-off and accelerated surface water run-back, which collectively reduce the ice-forming water flux that the heater must process.

2.3.2. Carbon-Based Electrothermal and Multifunctional Coatings

The integration of carbon-based conductive nanofillers into polymer matrices as intrinsic distributed heating elements has received growing attention as a route to eliminate the weight and geometric complexity penalties associated with embedded metallic resistive elements. Wang et al. [48] developed and tested a fluorine-modified carbon nanotube (CNT)-based self-heating superhydrophobic coating specifically designed for UAV propeller blade geometries, demonstrating that the coupled electrothermal and hydrophobic functionality enables anti-icing performance at significantly lower power densities than conventional film heater approaches. Their coating achieved water contact angles above 150° alongside surface resistivities below 500 Ω/sq, confirming the feasibility of the dual-function design. The percolation threshold in CNT-epoxy composites relevant to this application was characterised as occurring at MWCNT concentrations of 0.5–1.0 wt.%, above which the electrical conductivity increases by several orders of magnitude through the formation of a continuous nanotube network [48].

 doi:10.20944/preprints202605.0798.v1

2.3.3. Piezoelectric De-Icing Systems

Villeneuve et al. [15] demonstrated the feasibility of electromechanical de-icing for rotary-wing systems using piezoelectric actuators with an intermediate rubber layer, which amplifies the transmitted vibration amplitude into the blade substrate while providing electrical isolation. The system achieved complete de-icing at power densities one to two orders of magnitude below those required for electrothermal heating, with a characteristic de-icing cycle time of 0.5–2 s. The rubber interlayer concept is directly transferable to UAV composite propeller structures through the integration of polyvinylidene fluoride (PVDF) laminates or Macro Fibre Composites (MFC), whose flexibility permits conformal adhesion to the tapered, twisted geometry of small-scale blades without structural compromise.

2.4. Regulatory Framework and Critical Research Gaps

Current aeronautical regulations (FAR Part 25 Appendix C; EASA CS-25) define icing envelopes for certified crewed aircraft based on the Appendix C continuous-maximum and intermittent-maximum cloud envelopes. A subsequent amendment introduced Appendix O to address Supercooled Large Droplet (SLD) conditions [28]. However, no equivalent standard exists specifically for UAVs that establishes reference icing envelopes, minimum IPS performance requirements, or certification test methodologies [39]. This regulatory void constitutes a significant obstacle to expanding UAV operational envelopes under known icing conditions and has been identified as one of the most urgent priorities for standardisation bodies, air forces and research institutions [11].

The integration of the preceding review evidence identifies six specific research gaps that remain unresolved and motivate the present analysis: (1) the absence of validated electrothermal models that correctly account for laminar-to-turbulent boundary layer transition at UAV propeller Reynolds numbers; (2) the lack of systematic experimental ice accretion datasets for rotating propellers at $Re < 10^4$, representative of inner-span blade sections; (3) the insufficient characterisation of icephobic coating durability under the combined action of centrifugal stress, high-velocity erosion and repeated icing-de-icing cycling; (4) the limited understanding of the coupling between droplet collection efficiency and aeroelastic blade deformation under ice-induced imbalance loads; (5) the absence of standard UAV icing certification envelopes and associated test protocols; and (6) the scarcity of studies addressing the acoustic signature modification induced by propeller icing, which constitutes an operationally critical parameter in ISTAR-mission UAV platforms.

Table 1 summarises the most relevant contributions identified in the review, organised chronologically by thematic area.

Table 1. Key Contributions in the Literature on UAV and UAV Propeller Icing, Surface Materials, and Electrothermal Mitigation Systems.

Reference	Area	Main contribution	Method
[9]	UAV ops.	First documentation of icing on UAVs; failure mode identification	Operational analysis
[8]	Aerodynamics	Systematic C_L/C_D degradation quantification as a function of ice geometry	Literature review
[41]	SHC materials	Design principles for nanostructured icephobic surfaces	Experimental
[18]	Electrothermal	Surrogate-based optimisation of pulsed de-icing; 40–60 % energy reduction	CFD + optimisation

 doi:10.20944/preprints202605.0798.v1

Table 1. *Cont.*

Reference	Area	Main contribution	Method
[40]	Heat transfer	Unsteady Nu distribution over icing aerofoil; laminar separation effects	Experimental IWT
[31]	UAV review	Low-Reynolds icing research gaps for UAV platforms	Literature review
[14]	Propeller	Aerodynamic penalties from multi-rotor propeller icing; vibration failure modes	Experimental
[11]	UAV review	Comprehensive low-Reynolds propeller icing survey; dataset inventory	Literature review
[15]	Piezoelectric	Electromechanical de-icing for rotary systems; 10–50$\times$ energy reduction	Experimental
[36]	Rotor icing	Experimental icing apparatus for hovering drones; torque vs. thrust degradation	Experimental IWT
[24]	Active IPS	Propeller-integrated heater feasibility; tip vs. mid-span power density criteria	CFD + experimental
[44]	SHC durability	Erosion-resistant polyurethane hydrophobic coating; IAS $<$ 50 kPa at 100 m/s	Experimental
[32]	Propeller IPS	Electrothermal IPS design and IWT validation; low-Re CHT discrepancy identified	CFD + experimental
[45]	Icephobic coatings	Systematic drone rotor coating effectiveness; passive-only insufficient for glaze ice	Experimental IWT
[39]	Rotary UAV review	87-study survey; four unresolved UAV icing research gaps	Literature review
[47]	Hybrid IPS	SHC + heating hybrid reduces IPS power $>$ 80 % vs. continuous heating	Experimental IWT
[46]	Wettability	Hydrophobicity effects on ice shedding over rotating propeller	Experimental
[48]	CNT coatings	CNT self-heating SHC for UAV propeller blades; dual electrothermal-hydrophobic	Experimental
[33]	CHT simulation	Transition-aware CHT reduces predicted IPS power 15–25 % vs. fully turbulent	CFD
[37]	Forward flight	Advancing-blade asymmetric glaze accumulation under crosswind; IPS zone priority	Experimental IWT
[43]	Coating durability	Review of icephobic coating durability; smooth hydrophobic surfaces outperform SHS	Literature review
[34]	Propeller icing	Systematic MVD/LWC/T parametric study; MVD dominant; net drag at 60 μm	Experimental IWT
[38]	Full vehicle	Full quadcopter icing experiment; ESC current as ice detection proxy	Experimental

3. Atmospheric Ice Formation Mechanisms

3.1. Supercooled Liquid Water and Critical Parameters

The necessary condition for in-flight icing is the presence of Supercooled Liquid Water (SLW): droplets that remain in the liquid state at temperatures below 0 °C in the absence of efficient freezing nuclei [49,50]. Water can remain liquid down to approximately −40 °C; below this threshold homoge-

 doi:10.20944/preprints202605.0798.v1

neous nucleation is spontaneous. In the range from 0 °C to −40 °C, SLW droplets are commonly found in clouds and precipitation, constituting the critical range for aeronautical icing [51].

On impact with a surface whose temperature is below the freezing point, SLW droplets solidify forming ice accumulations whose geometry and adhesion depend on [52]:

- liquid water content in the cloud (LWC, g/m^3);
- median volumetric droplet diameter (MVD, μm);
- free-stream air temperature T_∞ (°C);
- relative airspeed (m/s);
- geometry of exposed surfaces.

The most severe conditions correspond to large-diameter droplets (Supercooled Large Droplets, SLD), present in freezing rain and freezing drizzle, which generate rapid glaze ice accumulations of high adhesion [52]. SLD conditions are particularly hazardous for UAVs because their thin blade profiles and short chord lengths fall outside the envelope of existing protection standards.

3.2. Classification of Aeronautical Ice

Three types of ice are recognised in aeronautics, with distinct characteristics and effects [6]:

Glaze ice (clear). Formed when relatively large water droplets impact the surface and freeze slowly, spreading before solidifying. The result is a dense, transparent, highly adhesive layer capable of forming the so-called *horn ice*: leading-edge protuberances that severely disrupt the flow. It is the most dangerous type due to its mechanical strength and difficulty of removal. On UAV propellers, glaze ice formation is particularly critical at moderate temperatures (−2 to −10 °C) combined with high LWC.

Rime ice (white). Produced when very small droplets freeze instantaneously on impact. It presents a porous, opaque structure, accumulating on leading edges. Although more brittle than glaze ice, its elevated formation rate makes it significant at very low temperatures (< -15 °C). Its brittleness provides a relative advantage for centrifugal expulsion strategies.

Mixed ice. A combination of the two preceding types. It presents irregular shapes that can significantly alter the aerodynamic flow, with intermediate adhesion and geometry properties. Mixed ice conditions are the most common in the altitude range (1000–4000 m) where most UAV tactical missions are conducted.

3.3. Cloud Types and Favourable Meteorological Conditions

Clouds are the primary reservoir of SLW and determine icing potential according to their type and altitude [53]:

High clouds (above 6000 m): cirrus, cirrostratus and cirrocumulus, composed mainly of ice crystals, present low risk of structural icing, as crystals tend not to adhere to surfaces.

Mid-level clouds (2000–6000 m): altostratus and altocumulus, may contain a mixture of liquid droplets, ice crystals and supercooled droplets. They represent potential conditions for prolonged icing, especially in extensive altostratus layers [6].

Low clouds (below 2000 m): stratus, stratocumulus, nimbostratus and cumulus, composed predominantly of liquid droplets. In winter conditions they may contain high concentrations of SLW, making them particularly favourable environments for aircraft icing. Nimbostratus clouds, associated with continuous precipitation at temperatures below 0 °C, generate especially severe icing conditions [52].

The most favourable meteorological conditions for in-flight icing occur in extensive stratiform clouds, warm fronts, freezing precipitation, freezing fog, and cumulonimbus with large concentrations of supercooled droplets [52].

4. Effects of Icing on UAV Propellers

UAV propellers operate under aerodynamic conditions substantially different from those of crewed aviation. With RPM values between 3000 and 15000, thin blade profiles and $Re = 10^4$–10^5, an

 doi:10.20944/preprints202605.0798.v1

ice accumulation of only 0.5–1 mm can degrade C_L by 30–40 % [8,14]. Table 2 presents a comparison of the icing effects between commercial aircraft and UAVs.

Table 2. Comparative Effects of Icing on Commercial Aircraft vs.UAVs.

Parameter	Commercial aircraft	UAV
Critical thickness	∼10–30 mm	0.5–1 mm
C_L reduction	5–15 %	30–40 %
Detection	On-board pilot	Autonomous system
Anti-icing energy	High (APU)	Limited (battery)
Regulation	FAR 25 / CS-25	Not consolidated
Acoustic signature	Not critical	Critical (ISTAR)

Specific icing effects on UAV propellers include five interconnected failure mechanisms. First, aerodynamic efficiency loss results from blade profile distortion, which modifies the local angle of attack and increases form drag. Second, dynamic imbalance arises from asymmetric accumulation between blades, generating vibrations capable of damaging motors and bearings; Hann et al. [14] identified this as a leading cause of propulsion-related mission aborts in cold-weather trials. Third, increased power consumption occurs as the flight controller attempts to compensate the thrust deficit by increasing motor current, accelerating battery depletion and potentially exceeding the thermal ratings of electronic speed controllers. Fourth, ice fragment shedding can impact sensors and cameras, generating debris that temporarily or permanently impairs mission-critical payloads. Fifth, acoustic signature alteration constitutes an operationally critical aspect in Intelligence, Surveillance and Reconnaissance (ISTAR) missions, where propeller noise must remain below detection thresholds.

The interaction between these failure modes makes the icing threat non-linear: at moderate ice accumulations, thrust loss dominates, but as imbalance grows, structural vibration may cause motor bearing failure before aerodynamic limits are reached. This underscores the need for early detection and mitigation systems capable of acting at ice thicknesses well below 1 mm.

4.1. Electrothermal Modelling

4.1.1. Thermodynamic Foundations: the Messinger Framework

The thermodynamic basis of ice accretion and electrothermal protection models was established by Messinger [1], who formalised the surface energy balance on an unheated body exposed to supercooled droplet impingement. The central concept introduced in that work is the *freezing fraction* n_0, defined as the ratio of the mass flux of water that freezes at the impingement surface to the total impinging mass flux:

$$n_0 = \frac{\dot{m}_{freeze}}{\dot{m}_{imp}} = \frac{\dot{m}_{imp} - \dot{m}_{runback}}{\dot{m}_{imp}} \tag{1}$$

When $n_0 = 1$, the regime is rime (all impinging water freezes instantaneously); when $0 < n_0 < 1$, glaze ice forms with a residual liquid film running back along the surface. This distinction is critical for electrothermal system design: anti-icing systems must supply sufficient heat flux to maintain $n_0 = 0$ at every chord station, while pulsed de-icing systems exploit $n_0 < 1$ to create a thin melt layer at the substrate interface without evaporating the full water catch. Myers [54] extended the original Messinger model to include temperature distributions within both the ice and water layers, producing the Extended Messinger Model (EMM) that is the standard thermodynamic kernel in modern codes such as FENSAP-ICE, LEWICE 3.2, and IGLOO2D [4,55].

4.1.2. Governing Equation for Electrothermal Ice Protection

Electric heating anti-icing is based on maintaining the blade surface above 0 °C, or generating thermal pulses that melt the ice-blade interface by driving $n_0 \to 0$ locally. The energy balance for the coupled system is [30]:

 doi:10.20944/preprints202605.0798.v1

$$\dot{Q}_{gen} = \dot{Q}_{conv} + \dot{Q}_{evap} + \dot{Q}_{sublim} + \dot{Q}_{accum} \tag{2}$$

where $\dot{Q}_{gen} = P = I^2R$ is the electrical power dissipated by the resistive elements, $\dot{Q}_{conv}$ represents the forced-convection losses to the airstream, $\dot{Q}_{evap}$ and $\dot{Q}_{sublim}$ are the latent heat terms associated with liquid evaporation and solid sublimation of surface water respectively, and $\dot{Q}_{accum}$ is the sensible heat stored in the blade thermal mass during transient operation. In anti-icing mode, $\dot{Q}_{accum} \to 0$ at steady state; in de-icing mode it is non-negligible during the heating pulse.

The governing partial differential equation for the discretised blade, treated as a continuum solid with embedded volumetric heat sources, is derived from Fourier conduction coupled with the surface boundary conditions [18]:

$$\rho c_p \frac{\partial T}{\partial t} = \nabla \cdot (k \nabla T) + \dot{q}_{elec} - h_{conv}(T - T_\infty) - \dot{q}_{ice} \tag{3}$$

where ρ, c_p and k are the blade material density, specific heat capacity and thermal conductivity; $\dot{q}_{elec}$ is the volumetric electrical power dissipated by the resistive elements; h_{conv} is the local convection coefficient [$\mathrm{W\,m^{-2}\,K^{-1}}$]; T_∞ is the free-stream air temperature; and $\dot{q}_{ice}$ is the latent heat sink associated with the phase change of the accretion. In composite CFRP or thermoplastic blade structures, k is a tensorial quantity that must account for the orthotropic thermal conductivity of the laminate; the in-plane conductivity ($k_{\parallel} \approx$ 1–5 $\mathrm{W\,m^{-1}K^{-1}}$) differs by one to two orders of magnitude from the through-thickness value [30], a distinction that critically affects the spatial uniformity of the heating distribution [32].

The term $\dot{q}_{ice}$ couples Equation (3) to the ice accretion thermodynamics through the freezing fraction n_0:

$$\dot{q}_{ice} = n_0 \cdot \dot{m}_{imp} \cdot L_f + (1 - n_0)\, \dot{m}_{imp}\, c_{p,w}(T_s - T_\infty) \tag{4}$$

where $L_f = 334\,\mathrm{kJ/kg}$ is the latent heat of fusion of water, $c_{p,w}$ is the specific heat of liquid water and T_s is the surface temperature. The coupled system formed by Equations (2)–(4) must be solved iteratively at each time step, since n_0 depends on T_s and T_s in turn depends on $\dot{q}_{ice}$ [55]. Modern simulation tools such as ANSYS FENSAP-ICE use finite-element spatial discretisation with Crank-Nicolson time integration for this coupled system, allowing the simultaneous prediction of ice shape evolution and required heating power in both anti-icing and de-icing modes [32,33].

4.1.3. Convection Coefficient on Rotating Propeller Blades

In UAV propellers, h_{conv} is highly non-uniform. It increases monotonically towards the blade tip due to the increase in local relative velocity:

$$V_{rel}(r) = \sqrt{(\Omega r)^2 + V_\infty^2} \tag{5}$$

where Ω is the angular velocity [rad/s] and r is the radial station. At the tip ($r \to R$), V_{rel} can reach 40–80 m/s for UAV operating at 6000–12000 RPM, placing the local Reynolds number in the range $Re_c = \rho V_{rel} c/\mu \approx 0.5$–$3 \times 10^4$ for typical blade chord values of $c =$ 8–20 mm.

In this regime, classical Dittus-Boelter and Nusselt-type correlations developed for high-Reynolds turbulent flow overestimate h_{conv} by factors of 2–4, as the boundary layer remains predominantly laminar along most of the blade chord [32,33]. The laminar flat-plate correlation:

$$Nu_x = 0.332\, Re_x^{1/2}\, Pr^{1/3}, \qquad Re_x = \frac{\rho V_{rel}\, x}{\mu} \tag{6}$$

provides a better first approximation but still neglects the effects of the leading-edge stagnation region, the favourable pressure gradient along the chord, and the possible laminar separation bubble that is known to occur on thin propeller profiles at low Reynolds numbers. Müller et al. [32] demonstrated through FENSAP-ICE conjugate heat transfer simulations that using a fully turbulent boundary

 doi:10.20944/preprints202605.0798.v1

layer assumption leads to overprediction of the required IPS heating power by 20–30% compared to transition-sensitive turbulence models, directly confirming that h_{conv} computed with high-Reynolds correlations is not appropriate for UAV applications.

The determination of experimentally validated $h_{conv}(r, x/c)$ distributions specific to the $Re = 10^4$–10^5 range and UAV blade geometries constitutes the most critical modelling gap identified in the present review and the primary input required for any power-optimal IPS design. Frey et al. [33] recently demonstrated that CHT simulations incorporating the k–ω Shear Stress Transport (SST) transition model reduce the discrepancy between predicted and experimentally measured anti-icing heat fluxes from 35% to below 15%, establishing SST as the minimum turbulence modelling fidelity required for UAV IPS design.

4.1.4. Continuous vs. Pulsed Heating Strategies

Three operational architectures for electrothermal IPS are relevant to UAV platforms, distinguished by their heat flux temporal profile and operational objective. Table 3 summarises the comparative characteristics.

Table 3. Thermal Control Strategies for UAV Anti-icing Systems.

Strategy	Mechanism	Rel. efficiency	Application
Continuous	$T_{blade} \geq 0\,^{\circ}\mathrm{C}$ permanent	1×	Short missions
Pulsed	Short high-power cycles to melt interface	3–5×	Long missions
Adaptive	Ice-sensor-triggered activation	Optimal	Autonomous systems

Continuous Anti-Icing Mode

In continuous mode the entire leading-edge zone is maintained at or above the freezing point at all times. This eliminates ice accretion completely but imposes a high steady-state power demand because the aerodynamic convection continuously extracts heat from the blade surface. Thomas et al. [30] showed that the required surface heat flux in fully evaporative continuous anti-icing mode can reach 10–40 $\mathrm{kW/m^2}$ depending on airspeed and ambient temperature, values that are energetically prohibitive for battery-powered UAV with typical power budgets of 50–200 W. Karpen et al. [24] confirmed this constraint for multirotor drone propellers, quantifying the anti-icing heat flux at the blade tip region as 1.5–3 $\mathrm{W/cm^2}$ and noting that this exceeds the total available power margin of small-scale platforms at their design point.

Pulsed De-Icing Mode

In pulsed (cyclic) de-icing mode, ice is permitted to accumulate to a critical thickness δ^*_{ice} before a high-power heating pulse of duration Δt_{pulse} melts a thin liquid film at the ice-substrate interface. The centrifugal acceleration at the blade tip, which can reach 10^3–$10^4\ g$ for UAV at high RPM, then expels the de-bonded ice mass [15,18]. The energy consumed per de-icing cycle is:

$$E_{pulse} = \int_0^{\Delta t_{pulse}} P_{elec}(t)\,\mathrm{d}t \approx \rho_{ice}\,\delta_{melt}\,L_f\,A_{heater} \tag{7}$$

where δ_{melt} is the melt-layer thickness required to reduce adhesion below the centrifugal expulsion threshold, typically 0.1–0.5 mm. Since only this thin interfacial layer needs to be melted rather than the full ice accumulation, pulsed de-icing consumes 3–5 times less energy than continuous anti-icing under the same icing conditions [18]. Hann et al. [14] confirmed experimentally that pulsed heating at $q_{pulse} \approx 3$–$5\ \mathrm{W/cm^2}$ over 0.5–2 s achieves complete ice shedding on an RG-15 UAV wing profile, while Wallisch and Hann [56] characterised the ice shedding time as a monotonically decreasing function of the applied heat flux, providing empirical design charts directly applicable to UAV IPS sizing. Samad et al. [57] extended these results to a hovering drone rotor configuration, measuring the heat loads required for electrothermal de-icing as a function of LWC, temperature and RPM, and demonstrating

 doi:10.20944/preprints202605.0798.v1

that the required heat flux increases non-linearly with LWC due to the enhanced convective loss associated with the larger wetted mass flux.

A critical consideration for pulsed de-icing on rotating blades is the *parting strip* architecture, in which a continuously heated narrow zone at the leading edge stagnation line prevents the re-adhesion of shed ice fragments and inhibits re-freezing of runback water in zones adjacent to the actively de-iced region [55]. Without a parting strip, runback ice ridges form aft of the heater zone and can generate aerodynamic penalties comparable to the original accretion [14].

Adaptive Mode

Adaptive IPS activates the heater only when ice detection algorithms identify a threshold accretion. The thermal signal from the heater zones themselves can serve as an ice detection mechanism: the surface temperature under a given power input is measurably lower when ice is present due to the additional thermal resistance and latent heat absorption, a principle demonstrated experimentally at low Reynolds numbers by Hann et al. [14] and implemented in the D·ICE commercial system. Integration with machine-learning ice detection algorithms using ESC current signatures—as demonstrated by Ercan and Dalkın [38] for a hovering quadcopter—enables closed-loop IPS activation without dedicated sensing hardware, a significant advantage for the severely mass-constrained UAV platform.

4.1.5. Power Optimisation of the IPS

The formal statement of the IPS optimisation problem is:

$$\min_{\mathbf{x}} \; E_{IPS} = \int_0^{t_m} P_{elec}(\mathbf{x}, t)\, \mathrm{d}t \tag{8}$$

$$\text{subject to:} \quad T_{blade}(r, t) \geq T_{lim}, \quad \forall\, r \in [r_{root},\, r_{tip}] \tag{9}$$

where the design variable vector $\mathbf{x}$ spans: the spatial distribution of heater zones and their individual resistances; the pulse peak power P_{peak}; the pulse duration Δt_{pulse}; the inter-pulse interval Δt_{rest}; and the parting-strip continuous power fraction. t_m is the mission duration and T_{lim} is the minimum allowable surface temperature, set to 0 °C for anti-icing or to the adhesion-failure temperature for de-icing. Inequality constraint (9) is evaluated at every radial station r and every time instant during the mission.

Pourbagian and Habashi [18] solved an analogous problem for fixed-wing aircraft leading edges using surrogate models (radial basis function metamodels) trained on FENSAP-ICE simulations, demonstrating energy reductions of 40–60% relative to continuous mode. Gallia et al. [58] presented a complementary framework using the MADS (Mesh Adaptive Direct Search) gradient-free optimiser coupled to the PoliMIce ice accretion code, minimising heater power while constraining runback ice formation, and demonstrating that non-uniform heat flux distributions—with higher power density at the leading-edge stagnation and at the blade tip—reduce total power consumption by up to 25% compared to uniform flux designs. Both frameworks rely on accurate $h_{conv}(r, x/c)$ as a mandatory input, which returns the analysis to the low-Reynolds convection coefficient gap identified in Section V.B.

Solving this problem for UAV propeller geometries requires: (i) validated CFD fields providing $h_{conv}(r, x/c)$ and droplet collection efficiency $\beta(r, x/c)$ at the relevant Reynolds numbers; (ii) a thermally coupled blade structural model that accounts for the orthotropic conductivity of composite laminates; and (iii) an ice shedding criterion that correctly predicts the centrifugal adhesion failure threshold as a function of ice layer geometry and temperature. None of these three inputs has been rigorously validated for the $Re = 10^4$–10^5 regime, constituting the most pressing experimental and computational priority for UAV electrothermal IPS development.

 doi:10.20944/preprints202605.0798.v1

4.2. Functional Surface Materials

Surface engineering strategies for icing mitigation on UAV propellers fall into three mechanistically distinct categories: passive icephobic coatings, which act before ice formation; electrothermal composite materials, which generate distributed Joule heating within the blade structure; and electromechanical de-icing systems, which exploit resonant vibration to fracture the ice-substrate interface. Each category is analysed below with emphasis on the physical mechanisms, quantitative performance data and operational limitations specific to the UAV propeller context.

4.2.1. Superhydrophobic and Icephobic Coatings

Physical Mechanism and Wettability Theory.

A superhydrophobic surface (SHS) is characterised by an apparent water contact angle $\theta^* > 150$ and a sliding angle $\alpha < 10$, resulting from a composite solid-air-liquid interface in the Cassie-Baxter wetting state [41]. The equilibrium contact angle in this state is governed by:

$$\cos\theta^* = \phi_s \cos\theta_Y - (1 - \phi_s) \tag{10}$$

where ϕ_s is the fraction of the projected area in solid-liquid contact and θ_Y is the Young contact angle of the flat, chemically homogeneous reference surface. Minimising ϕ_s through hierarchical micro-nano surface texturing reduces both the nucleation site density for heterogeneous ice crystallisation and the solid-liquid interfacial energy available to sustain adhesion. The ice adhesion strength (IAS) on SHS can be reduced to values of $\tau_{ice} < 25$ kPa compared to $\tau_{ice} = 200$–1000 kPa on untreated metallic or composite surfaces [42], facilitating passive ice expulsion by the centrifugal acceleration at the blade tip.

The distinction between superhydrophobicity and icephobicity is critical and frequently misunderstood. Nistal et al. [43] demonstrated through a comprehensive meta-analysis of 162 published IAS datasets that a WCA > 150 is neither necessary nor sufficient for low ice adhesion: the dominant predictor of icephobicity is the *receding* contact angle θ_{rec}, which governs the contact line retraction dynamics that must precede ice detachment. Surfaces with moderate WCA (90°–150°) but high θ_{rec}—such as smooth elastomeric fluoropolymer coatings—consistently outperform SHS in repeated icing-deicing cycling and under frost formation conditions, where capillary condensation infiltrates the surface microstructure and drives a Cassie-to-Wenzel wetting transition, eliminating icephobicity [43]. This finding fundamentally challenges the design paradigm that equates maximum roughness with maximum icephobicity.

Coating Systems with Potential for UAV Propellers

Systems showing the greatest potential for UAV propeller applications include: (i) sol-gel coatings with hierarchically distributed SiO_2 and TiO_2 nanoparticles on fluorinated silicone binders; (ii) PVDF-PDMS multi-stage rough coatings applied by cold spray, which simultaneously provide superhydrophobicity and resistance to UV degradation; and (iii) fluorine-modified CNT-epoxy functional coatings that integrate electrothermal capability with the passive SHC mechanism [48]. Piscitelli et al. [59] recently characterised two sol-gel SHC formulations developed specifically for aeronautical composite substrates, demonstrating IAS reductions of 86–90% relative to commercial aeronautical paint (AkzoNobel reference) while maintaining the Cassie-Baxter state at -29°C in static icing conditions, confirming their icephobic potential at temperatures relevant to UAV operation.

The Durability Challenge Under Operational Erosion

The central barrier to SHC adoption in fielded UAV propeller systems is erosion durability. The surface microstructure responsible for the Cassie-Baxter state is mechanically fragile: at UAV blade tips where V_{rel} can exceed 80–150 m/s in high-RPM configurations, impacting rain droplets generate *water hammer pressure* at the impact site:

 doi:10.20944/preprints202605.0798.v1

$$P_{hammer} \approx \rho_w \, c_w \, V_{impact} \tag{11}$$

where ρ_w is water density, $c_w \approx 1500\,\mathrm{m/s}$ is the speed of sound in water and V_{impact} is the droplet impact velocity. At $V_{impact} = 80\,\mathrm{m/s}$ this yields $P_{hammer} \approx 120\,\mathrm{MPa}$, far exceeding the compressive yield strength of most polymeric SHC microstructure elements [60]. The consequence is progressive wetting transition from Cassie-Baxter to Wenzel state and irreversible loss of icephobicity. Wang et al. [44] addressed this constraint through the development of *slippery erosion-resistant polyurethane (SPU)* coatings incorporating fluorinated and PDMS surface-modifying polymers at 1–5 wt.% in an erosion-resistant polyurethane matrix. The resulting coatings achieved WCA of 100–115° and IAS $< 50\,\mathrm{kPa}$ while retaining surface integrity under simulated leading-edge erosion at 100 m/s, establishing a viable design pathway that sacrifices extreme hydrophobicity for the mechanical robustness required in high-V_{rel} environments.

4.2.2. Slippery Liquid-Infused Porous Surfaces (SLIPS)

SLIPS represent a mechanistically distinct alternative to SHC icephobicity. Rather than trapping air in a solid microstructure (Cassie-Baxter state), SLIPS replace the air with a *low-surface-energy lubricant* immobilised within a nanoporous or microporous scaffold [61]. The lubricant layer eliminates solid-ice contact entirely, replacing the solid-ice interface with a liquid-ice interface whose shear strength is governed by the lubricant viscosity rather than surface chemistry. IAS values of 6–20 kPa have been achieved on SLIPS fabricated on aerospace aluminium alloys by anodisation followed by Krytox GPL lubricant infusion [61], values approximately two to four times lower than the best-performing SHC formulations reported under equivalent test conditions.

The fundamental limitation of SLIPS is lubricant depletion under the centrifugal loading and aerodynamic shear characteristic of UAV propeller operation. Muhammed and Virk [39] reviewed experimental comparisons between SHS, SLIPS and Stress-Localised Anti-Icing (SLAIS) coatings on rotating propellers, concluding that SLIPS and SLAIS exhibited more consistent thrust performance than SHS due to shorter and more regular ice shedding intervals, but that lubricant replenishment imposes a practical operational constraint not present for SHC. Self-repairing SLIPS architectures incorporating excess lubricant reservoirs in the porous matrix have demonstrated retention of IAS $<$ 20 kPa after 150 icing-deicing cycles and 100 abrasion cycles under laboratory conditions [61], but neither these cycling numbers nor the abrasion intensities are representative of the full service life expected of an UAV propeller system in operational deployment.

Nistal et al. [62] fabricated SLIPS on aerospace alloy AA6061-T6 using electrospun PTFE fibre scaffolds infused with silicone lubricant and evaluated their IAS under glaze and rime conditions accreted in an icing wind tunnel, demonstrating values of $\tau_{ice} < 15\,\mathrm{kPa}$ regardless of ice type. The absence of ice-type sensitivity—which is a well-documented weakness of SHC under glaze conditions—constitutes a significant advantage for UAV operation, where the transition between rime and glaze regimes occurs frequently as a function of altitude and temperature.

4.2.3. Composites with Conductive Nanofillers

Percolation Network and Joule Heating Mechanism

The incorporation of graphene, multi-walled carbon nanotubes (MWCNT) or carbon black into thermosetting polymer matrices creates a three-dimensional conductive percolation network that enables uniform Joule heating throughout the bulk of the material. The volumetric power dissipation density is governed by:

$$\dot{q}_{elec} = \frac{J^2}{\sigma_e(T)} = \sigma_e(T)\, E_{field}^2 \tag{12}$$

where J [A/m^2] is the current density, E_{field} [V/m] is the applied electric field and $\sigma_e(T)$ is the composite electrical conductivity as a function of temperature. The *percolation threshold*—the minimum

 doi:10.20944/preprints202605.0798.v1

filler concentration at which conductivity increases by several orders of magnitude—occurs at MWCNT concentrations of 0.5–1.0 wt.% in epoxy matrices [48], above which the conductivity follows the power-law scaling:

$$\sigma_e \propto (c - c_p)^{\beta} \tag{13}$$

where c is the filler weight fraction, c_p is the percolation threshold and $\beta \approx 1.3$–2.0 is the critical exponent for a three-dimensional percolation network. At concentrations of 1–5 wt.%, the achievable conductivity of 0.1–10 S/m is sufficient to generate heat fluxes of 1–5 kW/m^2 at modest applied voltages (10–30 V), converting the blade structural laminate itself into a distributed resistive heating element without the weight, geometric complexity and delamination risk associated with embedded metallic foil heaters.

Dual-Function CNT-Based Self-Heating SHC

Wang et al. [48] developed a fluorine-modified CNT-based composite coating that simultaneously provides the electrothermal function and superhydrophobic surface properties, reporting WCA > 150 and surface resistivity below 500 Ω/sq in a single spray-applied layer. The coating was specifically designed for curved UAV propeller blade geometries, demonstrating that the soft composite layer conforms to the tapered and twisted blade profile without cracking under the cyclic centrifugal strain of rotation. Under icing conditions representative of continuous maximum icing (LWC = 0.5 g/m^3, MVD = 20 μm, $T = -10$°C), the combined passive-active mechanism reduced the required electrical power by approximately 60% compared to a thermal film heater of equivalent coverage area applied to an uncoated blade. Tu et al. [46] independently confirmed the synergistic effect of substrate hydrophobicity on ice shedding dynamics, demonstrating that hydrophobic substrates reduce the critical ice mass threshold for centrifugal detachment by up to 40% compared to hydrophilic surfaces, directly reducing the power budget required for pulsed de-icing operation.

CFRP Structural Integration and Design Considerations

For CFRP composite propeller blades, the CNT/epoxy functional layer can be co-cured with the structural laminate as an outermost ply, or applied as a secondary bonded layer on a cured substrate. The electrical circuit is completed through blade-root slip rings or brushless electromagnetic couplers—the latter having been demonstrated in prototype UAV IPS configurations by Müller et al. [32]. The through-thickness electrical resistance of the structural CFRP laminate provides a natural series resistance that must be accounted for in the circuit model, and the temperature dependence of $\sigma_e(T)$ introduces a *positive thermal feedback* risk: as the coating heats up, σ_e decreases (semiconducting behaviour of CNT networks near the percolation threshold), reducing $\dot{q}$ and stabilising the temperature without active control. This self-regulating characteristic is thermodynamically advantageous for anti-icing applications and distinguishes CNT composites from metallic film heaters, which exhibit nearly temperature-independent resistance.

4.2.4. Piezoelectric Materials for Resonant De-icing

Physical Mechanism of Vibratory De-Icing

Electromechanical de-icing systems exploit the resonant vibration of a piezoelectric actuator bonded to the blade structure to generate cyclic stresses at the ice-substrate interface. De-icing occurs when the transverse shear stress at the interface exceeds the adhesion strength of impact ice, which is approximately $\tau_{adh} = 200$–800 kPa for glaze ice and $\tau_{adh} = 50$–200 kPa for rime ice depending on temperature and formation conditions [22]. The fracture condition is:

$$\tau_{interface}(x,t) = \rho_{blade}\,\delta(x)\,\ddot{u}(x,t) > \tau_{adh} \tag{14}$$

where $\delta(x)$ is the local ice layer thickness, ρ_{blade} is the blade density and $\ddot{u}(x,t)$ is the local transverse acceleration generated by the resonant vibration mode. The energy efficiency advantage of this

 doi:10.20944/preprints202605.0798.v1

mechanism over electrothermal heating stems from the fact that only the thin interfacial adhesion layer (on the order of microns) needs to be fractured, not the entire ice volume melted [63].

PZT-Based Systems: Helicopter and Early UAV Heritage

The fundamental viability of ultrasonic de-icing for rotary-wing systems was established by Palacios et al. [22], who demonstrated instantaneous de-icing of impact ice (layer thickness $< 2\,\text{mm}$) using lead zirconate titanate (PZT) actuators bonded to a stainless-steel rotor blade leading edge, with power densities of $0.1\text{–}0.5\,\text{W/cm}^2$—one to two orders of magnitude lower than electrothermal anti-icing. Overmeyer et al. [64] extended this work to a centrifugal icing environment representative of helicopter operational conditions, validating the bondline design methodology and demonstrating ice shedding under combined ultrasonic excitation and centrifugal loading. Budinger et al. [63] developed analytical and numerical models for architecture tradeoff of ultrasonic IPS, establishing that the optimal excitation frequency minimises the required actuator power by matching structural resonance modes that produce high interfacial shear amplitudes with minimum reactive power dissipation.

PVDF and MFC Actuators for UAV Propeller Integration

Rigid PZT ceramics are poorly suited to UAV composite propeller blades due to their brittleness, high density and difficulty of conformal bonding to curved surfaces. Polyvinylidene fluoride (PVDF) films and Macro Fibre Composites (MFC) offer a compelling alternative. PVDF is a semi-crystalline polymer with a piezoelectric coefficient $d_{31} \approx -33\,\text{pC/N}$, approximately 30 times lower than PZT-5A ($d_{33} \approx -130\,\text{pC/N}$), but its flexibility, low density ($\rho \approx 1780\,\text{kg/m}^3$), and ability to be laminated conformally onto complex-geometry composite structures make it the most compatible actuator material for UAV blade integration. Villeneuve et al. [15] demonstrated the effectiveness of a piezoelectric de-icing system for rotorcraft blades using a rubber interlayer between the actuator and the blade substrate, which amplifies the transmitted vibration amplitude and improves the coupling efficiency between the piezoelectric element and the host structure. MFC actuators, which consist of aligned PZT fibre arrays embedded in an epoxy matrix, achieve a compromise: $d_{33}^{eff} \approx 460\,\text{pC/N}$ in the fibre direction with sufficient flexibility for bonding to surfaces with radii of curvature down to approximately 30 mm.

Miao et al.[65] developed a systematic methodology for determining the optimal spanwise and chordwise position of MFC actuators on curved blade surfaces, using finite element modal analysis to identify the mode shapes that maximise interfacial shear stress at the leading edge while minimising input power. Their results demonstrated that actuator placement at the velocity antinode of the target mode, rather than at a maximum deflection node as is intuitively assumed, produces interfacial shear stresses 3–5 times higher for the same input power, a result with direct implications for UAV propeller IPS design.

Limitations and Interaction with Composite Blade Dynamics

The principal limitations of vibratory de-icing for UAV applications are: (i) *ice thickness threshold*: effective de-icing requires that the ice layer thickness be below approximately 2 mm for rime ice and somewhat less for glaze ice, since thicker layers exhibit resonance detuning effects that shift the structural modes and reduce the interfacial shear amplitude [22]; (ii) *composite-specific mode shapes*: CFRP propeller blades have anisotropic stiffness properties that produce mode shapes significantly different from the isotropic metallic plates on which most piezoelectric de-icing literature is based, requiring blade-specific FEA validation; and (iii) *fatigue in cyclic operation*: the repeated actuation at resonance frequencies introduces a cyclic fatigue loading into the adhesive bondline between the actuator and the blade, which must be accounted for in the structural certification of the IPS.

4.2.5. Comparative Analysis and TRL Assessment

Table 4 presents a comparative evaluation of the five surface strategies reviewed, including Technology Readiness Level (TRL) estimates referenced to the UAV propeller context specifically,

 doi:10.20944/preprints202605.0798.v1

which is more conservative than the general aerospace TRL for equivalent technologies applied to large-scale manned platforms.

Table 4. Comparative Overview of Surface Anti-icing and De-icing Strategies for UAV Propeller Blades. TRL estimates are specific to the UAV propeller context.

Technology	Weight penalty	Power demand	Mild icing	Severe icing	Key limitation (UAV)	TRL
SHC (micro+nano)	Minimal	None	High	Moderate	Erosion at tip ($V_{rel} >$ 80 m/s)	4–5
SLIPS	Minimal	None	High	High	Lubricant depletion under centrifugal load	3–4
SPU hydrophobic	Low	None	Moderate	Low–Mod.	Moderate IAS ($<$ 50 kPa) only	5–6
Thermal film	Low	High	Very high	Very high	Power budget on battery platforms	6–7
CNT/graphene	Minimal	Medium	High	High	Percolation stability; circuit integration	3–4
PVDF/MFC	Low	Very low	Medium	Limited	Ice $>$ 2 mm; composite mode detuning	3–4

The most technically mature passive strategy for immediate UAV deployment is the SPU hydrophobic coating (TRL 5–6), which sacrifices extreme icephobicity for the mechanical robustness required at high tip velocities [44]. The CNT/graphene functional composite represents the highest medium-term potential by combining the passive hydrophobic function with the active Joule heating function in a single conformal layer that adds negligible mass [48]. The vibratory de-icing approach via PVDF/MFC offers the lowest power demand but requires ice layer thickness to remain below $\sim$ 2 mm to remain effective, making it most suitable as a complementary mechanism within a hybrid IPS rather than a standalone system [63,65].

5. Discussion

5.1. Synthesis of Identified Scientific and Technological Gaps

The integrated review of Sections II–V reveals a pattern of interrelated gaps that collectively prevent the design of certifiable anti-icing systems for UAV propellers. Six critical gaps are identified, each more specific than previously published characterisations [11,39].

Gap 1 — Low-Reynolds electrothermal model fidelity. Existing conjugate heat transfer (CHT) codes, including FENSAP-ICE and IGLOO2D, were developed and validated for manned aircraft at $Re > 10^6$. When applied without modification to UAV propeller geometries ($Re = 10^4$–10^5), fully turbulent boundary-layer assumptions overestimate h_{conv} by 20–35%, leading to IPS designs with excess power requirements [32,33]. While Frey et al. [33] demonstrated that transition-aware k–ω SST models reduce this discrepancy to below 15%, the corresponding experimental validation datasets for

 doi:10.20944/preprints202605.0798.v1

rotating propeller geometries—as opposed to static aerofoils—remain essentially absent from the open literature. The blade rotation introduces additional complexity through the Coriolis and centrifugal body forces on the boundary-layer fluid and through the spanwise-varying relative velocity $V_{rel}(r)$, both of which invalidate the quasi-steady assumption implicit in most existing CFD tools.

Gap 2 — Propeller ice accretion characterisation dataset. Müller et al. [34] identified that fewer than 10 published experimental datasets existed for low-Reynolds propeller ice accretion at the time of their review, all with limited coverage of the MVD-LWC-temperature-RPM parameter space. Their parametric icing wind tunnel campaign addressed three MVD levels (20, 40 and 60 μm) and demonstrated that MVD is the dominant parameter, with the propeller generating net drag at MVD = 60 μm after only one minute of exposure. However, the operational envelope extends to LWC values above those tested and to temperatures below -15°C where rime ice dominates and the electrothermal modelling assumptions change significantly.

Gap 3 — Coating durability under operational conditions. Laboratory IAS measurements and icing wind tunnel tests, while necessary, are insufficient to qualify a coating for fielded UAV use. The combination of centrifugal erosion at blade-tip velocities $V_{rel} > 80$ m/s, sand and dust particle impacts in low-altitude operations, UV exposure at altitude, and repeated thermal cycling over hundreds of icing-deicing cycles constitutes a test environment that no existing coating has been qualified against at UAV propeller scale [43,60]. The transition from Cassie-Baxter to Wenzel state under water hammer pressure—quantified as $P_{hammer} \approx \rho_w c_w V_{impact}$—is a failure mode specific to high-V_{rel} applications for which neither SHC nor CNT/graphene composites have been systematically characterised.

Gap 4 — Ice shedding dynamics and blade aeroelastic coupling. Centrifugal expulsion is the primary de-icing mechanism for both pulsed electrothermal systems and vibratory de-icing systems on rotating UAV propellers. However, the critical ice mass threshold for expulsion depends on the radial ice distribution, the ice-substrate adhesion strength at operating temperature, and the local centrifugal acceleration $a_c = \Omega^2 r$, which at UAV tip radii and RPM values of 9000 rpm can exceed 10^3–$10^4\,g$. Asymmetric shedding between blades generates impulsive mass imbalance loads that excite blade bending and torsion modes, coupling the icing problem to the structural dynamics of the propeller. This coupling has been identified as a cause of vibration-induced motor failure [14] but has not been formally modelled in the UAV context.

Gap 5 — Acoustic signature under icing conditions. The acoustic output of a propeller is governed by the blade passage frequency, its harmonics, and the broadband noise from trailing-edge turbulence and blade-vortex interaction. Ice accretion modifies all three mechanisms: leading-edge ice distorts the blade loading distribution, altering the tonal signature; surface roughness from rime ice significantly increases broadband trailing-edge noise; and asymmetric accretion between blades generates new tonal components at the blade rotation frequency and its subharmonics. For ISTAR-mission UAVs operating at low altitude where acoustic detection is a primary threat, even modest icing-induced acoustic signature increases constitute an unacceptable tactical penalty [39]. No published study has quantified the acoustic signature modification of UAV propellers under controlled icing conditions.

Gap 6 — Regulatory and certification framework. Neither the FAA (FAR Part 25 Appendix C), EASA (CS-25 Amendment 16 Appendix O) [26] nor NATO STANAG standards currently provide icing envelopes, test methodologies or minimum IPS performance criteria specifically adapted to tactical UAV platforms. This absence prevents operational deployment under formally declared known icing conditions, restricting UAV employment to areas where icing can be operationally avoided [39].

5.2. Hybrid IPS as an Integrative Architecture

The comparative analysis of Sections III–V demonstrates that no single mitigation strategy is sufficient to cover the full UAV operational space under icing conditions. The functional limitations of each strategy are mechanistically complementary: SHC are effective under mild icing but fail under glaze ice with high LWC; continuous electrothermal heating is thermodynamically reliable but energetically prohibitive on battery platforms; pulsed de-icing is energy-efficient but loses effectiveness

 doi:10.20944/preprints202605.0798.v1

as ice thickness exceeds $\sim 2\,\text{mm}$; and vibratory de-icing is the lowest-power active option but is sensitive to ice layer geometry and blade resonance detuning.

The architecture that resolves these limitations is a three-layer hybrid IPS:

Layer 1 (passive baseline): a CNT/graphene functional composite as the outermost blade surface, providing simultaneous passive icephobicity (WCA > 150, IAS $< 50\,\text{kPa}$) and the electrical infrastructure for active heating through the same material [48]. Under mild icing conditions (rime, LWC $< 0.3\,\text{g/m}^3$), this layer alone may be sufficient to delay or prevent critical ice accumulation through reduced adhesion and centrifugal expulsion.

Layer 2 (adaptive pulsed de-icing): a carbon-fibre distributed heating zone in the parting-strip configuration, activated by the ice detection system when Layer 1 alone cannot maintain thrust within acceptable limits. The optimal pulse parameters (P_{peak}, Δt_{pulse}, Δt_{rest}) are scheduled by an on-board algorithm as a function of the icing severity estimate, exploiting the energy optimisation framework of Pourbagian and Habashi [18] and the updated power density data from Karpen et al. [24] for propeller geometries. Pulsed operation in this configuration consumes 3–5$\times$ less energy than continuous anti-icing under equivalent icing conditions [18].

Layer 3 (ice detection and control): a real-time ice monitoring system using thermal or current-signature ice detection as demonstrated by Hann et al. [14] and Ercan and Dalkın [38], respectively. ESC current monitoring requires no additional hardware and is therefore the most attractive option for retrofit deployment. The control algorithm outputs a ternary decision: (i) no action required; (ii) activate pulsed de-icing; or (iii) restrict mission envelope (altitude, airspeed or duration).

Han et al. [47] demonstrated experimentally that the hybrid combination of an SHC base layer with electrothermal heating can reduce total IPS power consumption by more than 80% relative to a conventional thermal anti-icing strategy without a coating, primarily through the droplet bounce-off and accelerated runback mechanisms that reduce the water flux reaching the heater zone. This result, obtained on a NACA0012 aerofoil at the Iowa State University IRT, provides a quantitative upper bound on the energy savings achievable by the three-layer architecture proposed here for UAV propellers.

Figure 1 illustrates the conceptual architecture of the proposed hybrid system, showing the functional roles of each hardware layer and the information flow from the ice monitoring subsystem to the adaptive control layer.

 doi:10.20944/preprints202605.0798.v1

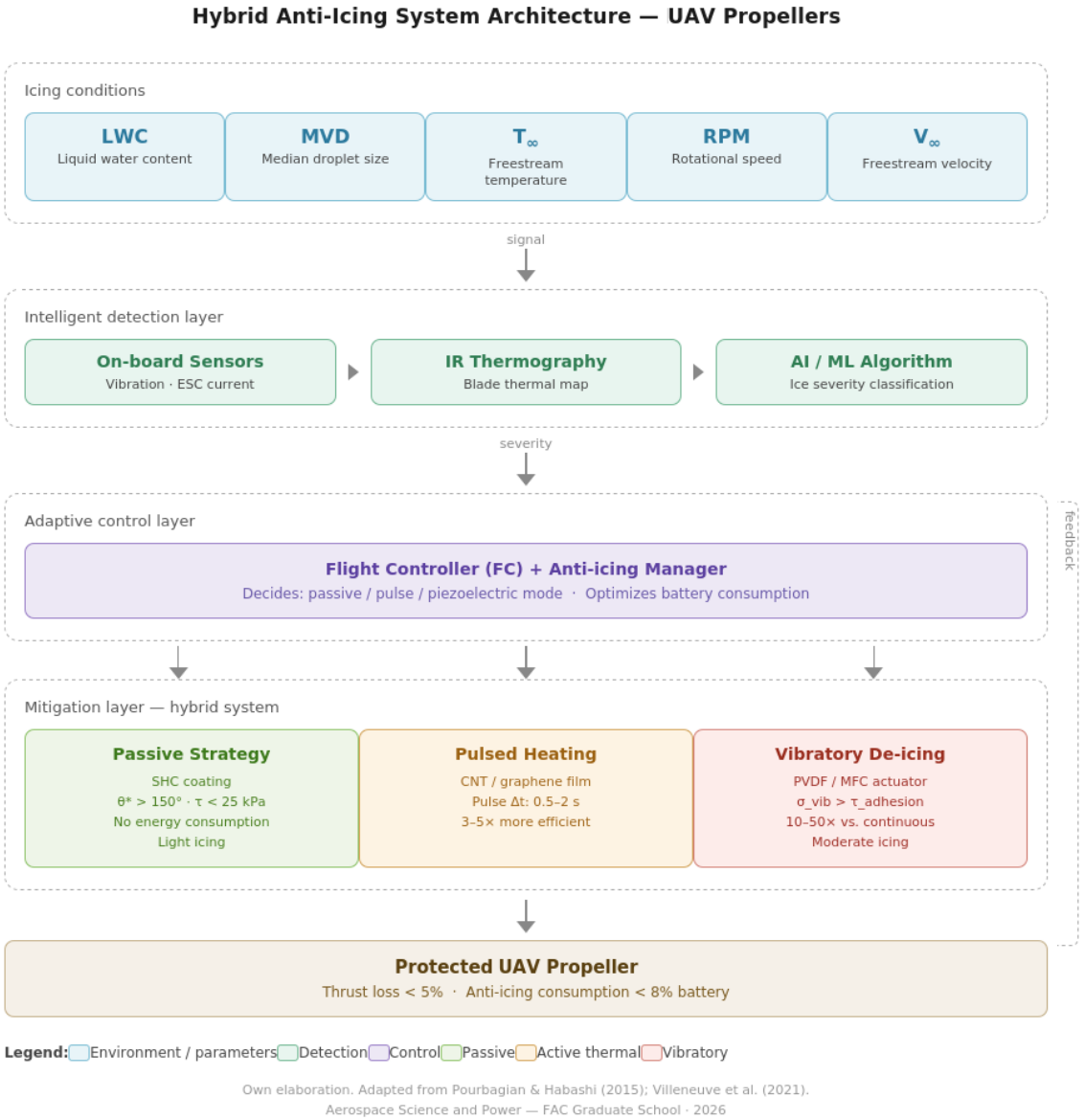

Figure 1. Conceptual architecture of the three-layer hybrid icing mitigation system for UAV propellers. Layer 1: passive CNT/SHC; Layer 2: adaptive pulsed de-icing; Layer 3: closed-loop ice detection and control. Source: own elaboration, adapted from [15,18,47].

5.3. Quantitative Implications for UAV System Design

The literature reviewed permits the construction of first-order design specifications for the proposed hybrid IPS on a representative small-to-medium UAV platform (propeller diameter 0.4–0.6 m, 6000–10000 RPM, battery-electric propulsion, $V_\infty = 15$–$30\,\mathrm{m/s}$):

Heating power density. Karpen et al. [24] established that the required anti-icing heat flux at the blade tip is 1.5–$3.0\,\mathrm{W/cm^2}$, approximately twice that required at mid-span due to the higher V_{rel} and collection efficiency. For a 0.5 m diameter, two-blade propeller, the total heater area in the leading 20% chord is approximately 60–$80\,\mathrm{cm^2}$, giving a total steady-state power demand of 90–240 W per propeller. In pulsed mode this reduces to 18–48 W mean power (at 3–5× efficiency advantage) [18], representing 5–12% of the typical 500 W rated power of a quad-rotor UAV drive system.

Coating weight penalty. A CNT/epoxy functional layer of 0.3–0.5 mm thickness and density $\rho \approx 1400\,\mathrm{kg/m^3}$ adds approximately 1.5–3 g per blade—well within the $< 5\%$ blade mass increase target [48].

 doi:10.20944/preprints202605.0798.v1

Expected thrust recovery. Müller et al. [34] demonstrated 100% thrust loss at MVD = 60 μm after one minute without protection. With the hybrid IPS, the combination of passive adhesion reduction and pulsed de-icing is expected to limit thrust loss to $< 5\%$ throughout a sustained icing encounter, consistent with the targets in Table 5.

Table 5. Expected Technological Impact Indicators of the Proposed Hybrid IPS for UAV Propellers. Reference icing condition: LWC = 0.5 g/m^3, MVD = 20 μm, $T_\infty = -10$°C, RPM = 8000.

Indicator	Baseline (no prot.)	Target (hybrid IPS)	Key reference
Thrust loss after 5 min	25–35 %	< 5 %	[34]
Mean IPS power (% of drive)	—	< 8 %	[24]
Ice adhesion [kPa]	200–1000	< 25	[48]
Saving vs. continuous heating	—	≥ 50 %	[47]
Blade mass increase	—	< 3 %	[48]
IAS after 500 icing cycles	N/A	< 50 kPa	[43]

5.4. Implications for Operations

The review results have direct implications across three phases of UAV employment.

Mission planning. The icing envelopes of Müller et al. [34] and Harvey et al. [37] provide the first empirically grounded data for go/no-go decision frameworks based on meteorological forecast parameters (temperature, LWC, MVD). For ISTAR missions, the additional constraint of acoustic signature degradation establishes a more conservative icing threshold than thrust loss alone, since acoustic detectability can be compromised before aerodynamic performance degrades to mission-limiting levels.

Platform design. Early selection of the CNT/graphene surface treatment and integration of the slip-ring electrical circuit is more mass- and cost-effective than retrofitting a full electrothermal IPS to a production platform. The design methodology of Gallia et al. [58] provides the optimisation framework for the non-uniform heat flux distribution that minimises battery energy consumption.

Logistics and airworthiness. The adoption of evidence-based coating inspection intervals requires characterisation of the Cassie-to-Wenzel transition rate as a function of cumulative tip velocity and environmental exposure. Until this data is available, conservative precautionary replacement intervals based on flight-hour thresholds are recommended, analogous to leading-edge erosion tape replacement on helicopter blades.

5.5. Prioritised Research Agenda

Based on the six gaps identified in Section VII.A, the following research priorities are recommended, in decreasing urgency:

Priority 1. Rotating propeller icing wind tunnel campaign at $Re = 10^4$–10^5 to generate experimental $h_{conv}(r, x/c)$ and $\beta(r, x/c)$ datasets for CFD validation. Conditions must span the full operational envelope: LWC 0.1–1.5 g/m^3, MVD 15–60 μm, T_∞ from -5 to -30°C, RPM 3000–12000, advance ratios representative of hover and forward flight modes [24,34].

Priority 2. Durability qualification of CNT/graphene and SPU coatings under simulated UAV blade-tip erosion at $V_{rel} = 80$–150 m/s, combined with thermal cycling over ≥ 500 icing-deicing events. This should produce service life charts and replacement interval criteria directly usable by UAV maintenance organisations [43,44].

Priority 3. Acoustic signature characterisation of iced UAV propellers under controlled IWT conditions, with and without IPS active, to quantify the ISTAR detectability penalty and establish minimum protection thresholds for stealth-sensitive missions.

Priority 4. Integrated ice detection and adaptive control system demonstration on a rotating propeller rig, validating the closed-loop IPS architecture described in Section VII.B and establishing the latency and false-alarm requirements for operationally acceptable ice detection [14,38].

 doi:10.20944/preprints202605.0798.v1

Priority 5. Engagement with NATO airworthiness bodies (e.g., STANAG 4671 framework) and national aviation authorities to initiate the development of icing envelopes, IPS qualification test procedures and minimum performance standards specific to tactical UAV platforms, analogous to the work done for civil aircraft under FAR Part 25 Appendix C and Appendix O [26,28].

5.6. Expected Impact Indicators

Table 5 summarises the expected technological impact indicators for the proposed hybrid system, based on consolidated data from the reviewed literature. The target values represent best-estimate performance bounds under continuous maximum icing conditions (LWC = 0.5 g/m^3, MVD = 20 μm, $T_\infty = -10$°C) for a representative small-to-medium UAV propeller operating at 8000 RPM.

6. Conclusions

This article has provided an integrated systematic review of atmospheric icing on UAV propellers, encompassing: the thermodynamic and aerodynamic mechanisms of ice accretion at low Reynolds numbers; the electrothermal modelling framework for heating system design and optimisation; and the functional surface material strategies available for passive and active icing mitigation. The following principal conclusions are drawn.

1. Icing on UAV propellers constitutes a qualitatively distinct and operationally more severe problem than on larger-scale crewed or commercial aircraft. The combination of low Reynolds numbers ($Re = 10^4$–10^5), thin blade profiles, severe energy constraints, and the absence of an on-board pilot capable of detecting and responding to progressive platform degradation means that ice accumulations of only 0.5–1 mm can generate thrust losses of 30–40% [8] and complete loss of the platform at MVD = 60 μm within 60 seconds of icing exposure [34].

2. The experimental literature on low-Reynolds propeller icing, while growing significantly since 2020, remains critically sparse. The parametric space of icing conditions —particularly at temperatures below -15°C, advance ratios corresponding to high-speed forward flight, and combined LWC-MVD-RPM combinations—has not been systematically characterised in the open literature. This represents the primary experimental gap limiting certifiable IPS development [11,39].

3. Electrothermal modelling of UAV propeller IPS requires specific low-Reynolds boundary-layer models that correctly capture the laminar-to-turbulent transition on rotating blades. Existing FENSAP-ICE simulations with fully turbulent assumptions overestimate the required IPS power by 20–35% [32], resulting in over-designed systems that consume battery capacity unnecessarily. The k–ω SST model with transition correction reduces this error below 15% [33] and represents the minimum fidelity required for UAV IPS design.

4. Among passive surface strategies, CNT/graphene functional composites present the highest near-term potential for UAV propellers by combining passive icephobicity (WCA > 150, IAS < 50 kPa) with an intrinsic electrothermal function in a single conformal layer of negligible mass addition [48]. The self-regulating thermal behaviour near the percolation threshold is thermodynamically favourable for anti-icing applications. Slippery erosion-resistant polyurethane (SPU) coatings offer the best durability-icephobicity compromise for applications where blade-tip relative velocities exceed 80 m/s [44].

5. Pulsed electrothermal de-icing, combined with a CNT/SHC passive base layer, is the most energy-efficient active strategy for battery-powered UAV. The hybrid SHC + pulsed heating strategy has been demonstrated to reduce total IPS energy consumption by more than 80% relative to conventional continuous heating on a NACA0012 aerofoil [47], with analogous savings expected for propeller geometries pending dedicated experimental validation. The parting-strip architecture [55] is essential to prevent runback ice ridge formation adjacent to the de-iced zone.

6. Piezoelectric de-icing via PVDF or MFC actuators offers the lowest absolute power demand of any active strategy (10–50$\times$ lower than continuous heating) but is limited to ice accumulations below approximately 2 mm [22] and requires blade-specific FEA modal analysis for actuator placement [65].

 doi:10.20944/preprints202605.0798.v1

Its most effective role is as a complementary active layer in a hybrid IPS rather than as a standalone system.

7. The complete absence of regulatory standards for UAV icing certification—equivalent to FAR Part 25 Appendix C for crewed aircraft—represents both a technical and operational obstacle that no amount of engineering progress alone can resolve. Joint action by NATO standardisation bodies, national airworthiness authorities and the research community is required to develop UAV-specific icing envelopes, IPS qualification test procedures and minimum performance criteria [26,28].

The results of this review establish the scientific and engineering basis for a structured experimental and numerical research programme aimed at the development of certifiable anti-icing systems for UAV propellers. Addressing the six prioritised research gaps identified in Section VII.A would provide the validation data, design tools, coating qualification criteria and regulatory framework necessary to expand the operational envelope of tactical UAV platforms to include formally declared known icing conditions, contributing materially to the operational safety and mission effectiveness of these platforms in the Colombian Air Force and allied forces in high-latitude and mountainous operating theatres.

Author Contributions: **P. N. López**: Conceptualisation, literature review. **C. A. González**: Formal analysis, writing—original draft, writing—review and editing. **R. Avella**: Conceptualization, methodology, formal analysis, literature review, writing—original draft preparation, writing—review, editing and supervision.

Acknowledgments: The authors thank the support of Fundación Universitaria Los Libertadores, Faculty of Engineering and Basic Sciences, in the development of this review. This work is part of the research project "Icing Mitigation in UAV Propulsion Systems through Electrothermal Modelling and Functional Materials", affiliated with the Faculty of Engineering and Basic Sciences.

Conflicts of Interest: The authors declare no conflict of interest related to the publication of this article.

References

1. Messinger, B.L. Equilibrium temperature of an unheated icing surface as a function of air speed. *Journal of the Aeronautical Sciences* **1953**, *20*, 29–42. https://doi.org/10.2514/8.2520.
2. Bergrun, N.R. A Method for Numerically Calculating the Area and Distribution of Water Impingement on the Leading Edge of an Airfoil in a Cloud. Technical Report TN-1397, National Advisory Committee for Aeronautics (NACA), 1947.
3. Ruff, G.A.; Berkowitz, B.M. Users' Manual for the NASA Lewis Ice Accretion Prediction Code (LEWICE). Technical Report CR-185129, NASA Glenn Research Center, 1990.
4. Wright, W.B. User's Manual for LEWICE Version 3.2. Technical Report NASA/CR-2008-214255, NASA Glenn Research Center, 2008.
5. Habashi, W.G.; Dompierre, J.; Bourgault, Y.; Ait-Ali-Yahia, D.; Fortin, M.; Vallet, M.G. Certifiable computational fluid dynamics through mesh optimization. *International Journal for Numerical Methods in Fluids* **2004**, *44*, 727–748. https://doi.org/10.1002/fld.666.
6. Federal Aviation Administration (FAA). Pilot's Handbook of Aeronautical Knowledge. Technical Report FAA-H-8083-25B, U.S. Department of Transportation, 2016.
7. Lynch, F.T.; Khodadoust, A. Effects of ice accretions on aircraft aerodynamics. *Progress in Aerospace Sciences* **2001**, *37*, 669–767. https://doi.org/10.1016/S0376-0421(01)00018-5.
8. Bragg, M.B.; Broeren, A.P.; Blumenthal, L.A. Iced-airfoil aerodynamics. *Progress in Aerospace Sciences* **2005**, *41*, 323–362. https://doi.org/10.1016/j.paerosci.2005.07.001.
9. Siquig, R.A. Impact of Icing on Unmanned Aerial Vehicle (UAV) Operations. Technical Report TR-90-01, Naval Environmental Prediction Research Facility, 1990.
10. Kimura, S.; Nakamura, K.; Sato, H.; Yamamoto, T. Ice detection and anti-icing system for multirotor unmanned aerial vehicles using embedded sensors and electrothermal elements. *Drones* **2023**, *7*, 235. https://doi.org/10.3390/drones7040235.
11. Hann, R.; Wallisch, J. UAV icing: A review of current challenges and research needs. *SAE International Journal of Advances and Current Practices in Mobility* **2020**, *2*, 2960–2974. https://doi.org/10.4271/2020-01-0058.

 doi:10.20944/preprints202605.0798.v1

12. CANOLA, S.S.S.O. Measurement of droplet size distribution characteristics of a spray dryer-rotary atomizer using phase doppler anemometry technique. *Agricultural Engineering* **2010**, *13*, 04.
13. Kind, R.J.; Potapczuk, M.G.; Feo, A.; Golia, C.; Shah, A.D. Experimental and computational simulation of in-flight icing phenomena. *Progress in Aerospace Sciences* **1998**, *34*, 257–345. https://doi.org/10.1016/S0376-0421(98)00007-3.
14. Hann, R.; Enache, A.; Nielsen, M.C.; Stovner, B.N.; van Beeck, J.; Johansen, T.A.; Thorsen, K.A. Experimental heat loads for electrothermal anti-icing and de-icing on UAVs. *Aerospace* **2019**, *6*, 13. https://doi.org/10.3390/aerospace6020013.
15. Villeneuve, E.; Ghinet, S.; Volat, C. Improvement of the electromechanical de-icing system for rotorcrafts through the use of a rubber interlayer between the heating element and the structure. *Aerospace* **2021**, *8*, 96. https://doi.org/10.3390/aerospace8030096.
16. Ning, Z.; Luo, C.; Xu, S.; Xu, J.; Liu, C. Effect of ambient temperature on icing characteristics and aerodynamic performance of UAV aerofoil and rotor. *Aerospace Science and Technology* **2021**, *116*, 106878. https://doi.org/10.1016/j.ast.2021.106878.
17. Cao, Y.; Wu, Z.; Su, Y.; Xu, Z. Aircraft flight characteristics in icing conditions. *Progress in Aerospace Sciences* **2015**, *74*, 62–80. https://doi.org/10.1016/j.paerosci.2014.12.001.
18. Pourbagian, M.; Habashi, W.G. Surrogate-based optimization of electrothermal anti-icing systems in transient de-icing mode. *International Journal of Heat and Fluid Flow* **2015**, *54*, 54–67. https://doi.org/10.1016/j.ijheatfluidflow.2015.05.002.
19. Fortin, G.; Perron, J. Ice adhesion models to predict shear stress at shedding. In Proceedings of the Proceedings of the AIAA Atmospheric and Space Environments Conference, San Antonio, TX, USA, 2009; AIAA Paper 2009-4167. https://doi.org/10.2514/6.2009-4167.
20. Parent, O.; Ilinca, A. Anti-icing and de-icing techniques for wind turbines: Critical review. *Progress in Aerospace Sciences* **2011**, *47*, 16–26. https://doi.org/10.1016/j.paerosci.2010.06.001.
21. Brassard, J.D.; Sarkar, D.K.; Perron, J. Fluorine-based superhydrophobic coatings with silver nanoparticles for electrical de-icing systems. *Advanced Materials Interfaces* **2017**, *4*, 1600524. https://doi.org/10.1002/admi.201600524.
22. Palacios, J.L.; Smith, E.C.; Rose, J.; Royer, R. Ultrasonic de-icing of wind-tunnel impact icing. *AIAA Journal* **2011**, *49*, 1158–1167. https://doi.org/10.2514/1.J050344.
23. Scholz, P.; Möller, T.; Radespiel, R. Experimental and numerical investigation of leading-edge roughness effects on low-Reynolds airfoil performance. *Cold Regions Science and Technology* **2021**, *181*, 103177. https://doi.org/10.1016/j.coldregions.2020.103177.
24. Karpen, N.; Diebald, S.; Dezitter, F.; Bonaccurso, E. Propeller-integrated airfoil heater system for small multirotor drones in icing environments: Anti-icing feasibility study. *Cold Regions Science and Technology* **2022**, *201*, 103616. https://doi.org/10.1016/j.coldregions.2022.103616.
25. McCarty, M.F.; Khalid, M.O.; Brandt, J.B. Droplet impingement and ice accretion on small UAV propellers at low Reynolds numbers. *Journal of Aircraft* **2023**, *60*, 441–455. https://doi.org/10.2514/1.C037012.
26. European Union Aviation Safety Agency (EASA). Certification Specifications and Acceptable Means of Compliance for Large Aeroplanes CS-25, Amendment 16, Appendix O—Supercooled Large Droplet Icing Conditions. Technical report, EASA, Cologne, Germany, 2015.
27. Wright, W.B.; Rutkowski, A.; Potapczuk, M. Numerical Predictions for Experimental Clean-Up Icing Tests. Technical Report TM-107307, NASA Glenn Research Center, 1997.
28. Federal Aviation Administration (FAA). Appendix C to Part 25—Atmospheric Icing Conditions. Technical report, U.S. Department of Transportation, 2022. Code of Federal Regulations, Title 14, Part 25.
29. Gent, R.W.; Dart, N.P.; Cansdale, J.T. Aircraft icing. *Philosophical Transactions of the Royal Society A* **2000**, *358*, 2873–2911. https://doi.org/10.1098/rsta.2000.0689.
30. Thomas, S.K.; Cassoni, R.P.; MacArthur, C.D. Aircraft anti-icing and de-icing techniques and modeling. *Journal of Aircraft* **1996**, *33*, 841–854. https://doi.org/10.2514/3.47027.
31. Cao, Y.; Tan, W.; Wu, Z. Aircraft icing: An ongoing threat to aviation safety. *Aerospace Science and Technology* **2018**, *75*, 353–385. https://doi.org/10.1016/j.ast.2017.12.028.
32. Müller, N.C.; Løw-Hansen, B.; Borup, K.T.; Hann, R. UAV icing: Development of an ice protection system for the propeller of a small UAV. *Cold Regions Science and Technology* **2023**, *213*, 103938. https://doi.org/10.1016/j.coldregions.2023.103938.

 doi:10.20944/preprints202605.0798.v1

33. Frey, M.; Müller, N.C.; Wallisch, J.; Hann, R. UAV icing: Experimental investigation and numerical CHT simulations of a propeller ice protection system. In Proceedings of the Proceedings of the AIAA SciTech Forum, Orlando, FL, USA, 2024; AIAA Paper 2024-0871. https://doi.org/10.2514/6.2024-0871.
34. Müller, N.C.; Wallisch, J.; Borup, K.T.; Hann, R. UAV icing: Experimental characterization of the performance impact of ice accretion on a propeller. *Drones* **2025**, *10*, 166. https://doi.org/10.3390/drones10030166.
35. Shi, D.Z.; et al. Effect of icing parameter variations on propeller icing. *Journal of Applied Fluid Mechanics* **2026**, *19*, 499–519.
36. Villeneuve, E.; Samad, A.; Volat, C.; Béland, M.; Lapalme, M. Experimental investigation of icing effects on a hovering drone rotor performance. *Drones* **2022**, *6*, 345. https://doi.org/10.3390/drones6110345.
37. Harvey, D.; Villeneuve, E.; Béland, M.; Lapalme, M. Wind tunnel investigation of the icing of a drone rotor in forward flight. *Drones* **2024**, *8*, 380. https://doi.org/10.3390/drones8080380.
38. Ercan, H.; Dalkin, A. Full-vehicle experimental investigation of propeller icing on a hovering quadcopter. *Drones* **2025**, *9*, 729. https://doi.org/10.3390/drones9110729.
39. Muhammed, M.; Virk, M.S. Ice accretion on rotary-wing unmanned aerial vehicles—a review study. *Aerospace* **2023**, *10*, 261. https://doi.org/10.3390/aerospace10030261.
40. Liu, Y.; Hu, H. An experimental investigation on the unsteady heat transfer process over an ice accreting airfoil surface. *International Journal of Heat and Mass Transfer* **2018**, *122*, 707–718. https://doi.org/10.1016/j.ijheatmasstransfer.2018.02.023.
41. Mishchenko, L.; Hatton, B.; Bahadur, V.; Taylor, J.A.; Krupenkin, T.; Aizenberg, J. Design of ice-free nanostructured surfaces based on repulsion of impacting water droplets. *ACS Nano* **2010**, *4*, 7699–7707. https://doi.org/10.1021/nn102557p.
42. Susoff, M.; Siegmann, K.; Pfaffenroth, C.; Hirayama, M. Evaluation of icephobic coatings—screening of different coatings and influence of roughness. *Progress in Organic Coatings* **2013**, *76*, 1036–1040. https://doi.org/10.1016/j.porgcoat.2012.10.015.
43. Nistal, A.; Sierra-Martín, B.; Fernández-Barbero, A. On the durability of icephobic coatings: A review. *Materials* **2024**, *17*, 235. https://doi.org/10.3390/ma17010235.
44. Wang, X.; et al. Erosion resistant hydrophobic coatings for passive ice protection of aircraft. *Applied Sciences* **2022**, *12*, 9589. https://doi.org/10.3390/app12199589.
45. Villeneuve, E.; Samad, A.; Volat, C.; Béland, M.; Lapalme, M. Experimental assessment of the ice protection effectiveness of icephobic coatings for a hovering drone rotor. *Cold Regions Science and Technology* **2023**, *210*, 103858. https://doi.org/10.1016/j.coldregions.2023.103858.
46. Tu, J.; Tian, W.; Wang, X.; Tian, L. Experimental study on the effects of substrate hydro-/icephobicity on ice mitigation and ice shedding during the dynamic icing process over the rotating propeller of an unmanned aerial vehicle. *Aerospace Science and Technology* **2024**, *155*, 109610. https://doi.org/10.1016/j.ast.2024.109610.
47. Han, N.; Hu, H.; Hu, H. An experimental study to compare the effectiveness of superhydrophobic coating and icephobic coating for aircraft icing mitigation. In Proceedings of the Proceedings of the AIAA Aviation Forum, 2023, AIAA Paper 2023-4275. https://doi.org/10.2514/6.2023-4275.
48. Wang, J.; Frantz, J.; Chumbley, E.; Samad, A.; Valentin, C.; Hu, H. An explorative study on using carbon nanotube-based superhydrophobic self-heating coatings for UAV icing mitigation. *Molecules* **2025**, *30*, 3472. https://doi.org/10.3390/molecules30173472.
49. National Oceanic and Atmospheric Administration (NOAA). Cloud Classification and Characteristics. [Online]. Available: https://www.noaa.gov.
50. SKYbrary. In-Flight Icing. SKYbrary Aviation Safety. [Online]. Available: https://skybrary.aero/articles/flight-icing.
51. Farzaneh, M. *Atmospheric Icing of Power Networks*; Springer, 2008. https://doi.org/10.1007/978-1-4020-8530-4.
52. European Union Aviation Safety Agency (EASA). In-Flight Icing. Safety Information Leaflet SIL No. 2009-14R2, EASA, 2009.
53. World Meteorological Organization (WMO). *International Cloud Atlas*; Number WMO-No. 407, WMO, 2017.
54. Myers, T.G. Extension to the Messinger model for aircraft icing. *AIAA Journal* **2001**, *39*, 211–218. https://doi.org/10.2514/2.1300.
55. Trontin, P.; Blanchard, G.; Larrouturou, A.; Villedieu, P. Numerical simulation of an electrothermal ice protection system in anti-icing and deicing mode. *Aerospace* **2023**, *10*, 75. https://doi.org/10.3390/aerospace10010075.

 doi:10.20944/preprints202605.0798.v1

56. Wallisch, J.; Hann, R. UAV icing: Experimental investigation of ice shedding times with an electrothermal de-icing system. In Proceedings of the Proceedings of the AIAA Aviation Forum, 2022, AIAA Paper 2022-3905. https://doi.org/10.2514/6.2022-3905.
57. Samad, A.; Villeneuve, E.; Volat, C.; Béland, M.; Lapalme, M. Experimental assessment of the ice protection effectiveness of electrothermal heating for a hovering drone rotor. *Experimental Thermal and Fluid Science* **2023**, *149*, 110992. https://doi.org/10.1016/j.expthermflusci.2023.110992.
58. Gallia, M.; Gori, G.; Guardone, A. Numerical optimization of electrothermal ice protection systems. In *Handbook of Numerical Simulation of In-Flight Icing*; Habashi, W.G., Ed.; Springer: Cham, 2024; chapter 37. https://doi.org/10.1007/978-3-031-33845-8_37.
59. Piscitelli, F.; Fanciullo, M.; Sarcinella, A.; Costantini, M.; Frigione, M. Icephobic properties of superhydrophobic coatings developed for aeronautical applications. *Coatings* **2025**, *15*, 621. https://doi.org/10.3390/coatings15060621.
60. Nistal, A. Challenges in the durability of superhydrophobic coatings pertinent to unmanned aerial vehicle (UAV) icing mitigation. In *Superhydrophobic Coating—Recent Advances in Theory and Applications*; IntechOpen, 2024. https://doi.org/10.5772/intechopen.1006234.
61. Yuan, Y.; Xiang, H. Self-repairing performance of slippery liquid infused porous surfaces for durable anti-icing. *Advanced Materials Interfaces* **2022**, *9*, 2101968. https://doi.org/10.1002/admi.202101968.
62. Nistal, A.; Fernández-Barbero, A.; González-Martín, L. Icephobic coating based on novel SLIPS made of infused PTFE fibers for aerospace application. *Coatings* **2024**, *14*, 341. https://doi.org/10.3390/coatings14030341.
63. Budinger, M.; Pommier-Budinger, V.; Napias, G.; Costa da Silva, A. Ultrasonic ice protection systems: Analytical and numerical models for architecture tradeoff. *Journal of Aircraft* **2016**, *53*, 680–690. https://doi.org/10.2514/1.C033625.
64. Overmeyer, A.; Palacios, J.L.; Smith, E.C. Ultrasonic de-icing bondline design and rotor ice testing. *AIAA Journal* **2013**, *51*, 2965–2976. https://doi.org/10.2514/1.J052601.
65. Miao, B.; Li, W.; Yuan, L.; Zhu, C. Determining region of installation of flat-ended piezoelectric de-icing actuators on curved surfaces. *Journal of Aircraft* **2023**, *60*, 232–244. https://doi.org/10.2514/1.C036855.